DESIGN REPORT

#216

TEAM ASSAILING FALCONS

VELLORE INSTITUTE OF TECHNOLOGY

SAE AERO DESIGN EAST 2024

MARUT

ADHVAITH SHIVKUMAR
ADITYA MOHAN
DHRUV BOBBY JOHNSON
DHRUV TIBREWALA
DILJITH RAGESH
JAYWANT NITIN NIKAM
KAUSTUBH KUMAR
PRANEEL NIMBALKER
PRANJAL TALAPATRA
RAJ ALPESH PAREKH
REUBEN SHIBU GEORGE
RISHAB SAHNI
ROHAN ZACHARIAH PHILIP
RUGVED WADNERKAR
SAI TANUSHA PALLE
SAMARTH SAWANT
SHIVRAJ S NAIR
SHREYA
SHWETA KARPE
SOHAM DESHPANDE

APPENDIX A - STATEMENT OF COMPLIANCE

Certification of Qualification

Team Name	ASSAILING FALCONS	Team Number	216
School	VELLORE INSTITUTE OF TECHNOLOGY		
Faculty Advisor	DR. GUNDABATTINI EDISON		
Faculty Advisor's Email	g.edison@vit.ac.in		

Statement of Compliance

As faculty Adviser:

GE (Initial) I certify that the registered team members are enrolled in collegiate courses.

GE (Initial) I certify that this team has designed and constructed the radio-controlled aircraft in the past nine (9) months with the intention to use this aircraft in the 2024 SAE Aero Design competition, without direct assistance from professional engineers, R/C model experts, and/or related professionals.

GE (Initial) I certify that this year's Design Report has original content written by members of this year's team.

GE (Initial) I certify that all reused content have been properly referenced and is in compliance with the University's plagiarism and reuse policies.

GE (Initial) I certify that the team has used the Aero Design inspection checklist to inspect their aircraft before arrival at Technical Inspection and that the team will present this completed checklist, signed by the Faculty Advisor or Team Captain, to the inspectors before Technical Inspection begins.

12/1/2024

Signature of Faculty Advisor (EDISON GUNDABATTINI) — Date: 12th January 2024

Signature of Team Captain — Date: 12th January 2024

Note: **A copy of this statement needs to be included in your Design Report as page 2 (Reference Section 4.3)**

Table of Contents

Table of Figures

Table of Tables

Table of Acronyms

AC	Aerodynamic Center
AoA	Angle of Attack
AoI	Angle of Incidence
AR	Aspect Ratio
AVL	Athena Vortex Lattice
AZDN	Adaptive Zone Detection and Navigation
B	Balsa
C_D	Coefficient of Drag
CF	Carbon Fiber
CFD	Computational Fluid Dynamics
CG	Center of Gravity
C_L	Coefficient of Lift
DAS	Data Acquisition System
DVM	Dynamic Vector Mapping
ESC	Electronic Speed Controller
FG	Fibre Glass
FOD	Foreign Object Damage
FOM	Figure of Merits
FOS	Factor of Safety
FS	Flight Score

GLS	Guided Landing System
GTV	Ground Transport Vehicle
GUI	Graphical User Interface
HC	Honeycomb
H-stab	Horizontal Stabilizer
L/D	Lift to Drag Ratio
LE	Leading Edge
Li-Po	Lithium Polymer
MAC	Mean Aerodynamic Chord
MLG	Main Landing Gear
NLG	Nose Landing Gear
OD	Outer Diameter
P	Plywood
PA	Primary Aircraft
PADA	Powered Autonomous Delivery Aircraft
PLA	Polylactic Acid
R/C	Rate of Climb
t/c	Thickness to Chord Ratio
TE	Trailing Edge
TMD	Thrust Measuring Device
V_H	Horizontal Tail Volume Ratio
V-stab	Vertical Stabilizer
V_V	Vertical Tail Volume Ratio
x/c	Position to Chord Ratio

1. Executive Summary

Team Assailing Falcons presents this year's flagship, *Marut*, designed to compete in SAE Aero Design East 2024. Aligned with the mission, a system has been developed to combat wildfires using a Powered Autonomous Delivery Aircraft (PADA). This autonomous system is capable of securely transporting all elements of a Ground Transport Vehicle (GTV) through self-guided navigation. The aircraft integrates advanced aerodynamic features, high strength-to-weight ratio and neoteric avionics system achieved through extensive analyses and physical testing, as elucidated in this design report.

1.1 Conspectus

Marut is a mid-wing aircraft with a semi-tapered planform, lifting-body fuselage and a U-tail, propelled by a single motor, designed to carry 13.2 lbs of static payload. To increase its robustness, composites of Fiber Glass (FG) and Carbon Fiber (CF) laminates with either a Nomex Honeycomb (HC) or Balsa (B) core are strategically placed. It deploys a PADA, capable of autonomously landing in any given zone. It is designed to convert into a GTV with the ability of autonomous payload delivery.

$C_{L\ cruise}$	0.96
$C_L/C_{D\ cruise}$	9.26
$C_{L\ max}$	2.04
V_S	30.6 ft/s
Wing Loading	2.27 lbf/ft^2

Table 1.1 Key Performance Parameters

1.2 Mission Constraints

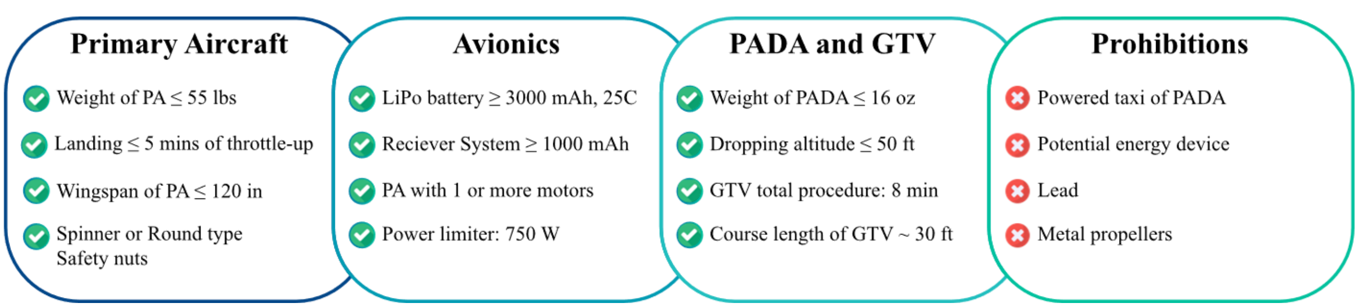

Figure 1.1 Advanced Class Constraints

1.3 Team Objectives

- Design an aircraft, according to the mission constraints and manufacturing feasibility, while maximizing the static payload capacity by developing a reliable design capable of high lift while minimizing aerodynamic resistance through optimization, utilizing a systems design approach.
- The PADA, after safe release from the Primary Aircraft (PA), should be able to transport the entire GTV relying on an autonomous system while adhering to the weight constraint.
- Develop an autonomous GTV designed for quick assembly with the capability to map the optimal path for payload delivery while complying with the specified time constraints.

1.4 Risk Assessment

The probability of occurrence and severity of consequences of major project risks were graded and quantified equipping the team for strenuous impediments as depicted in *Figure 1.2*.

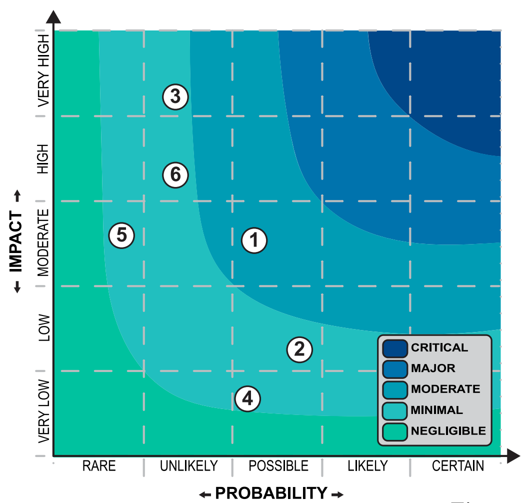

	Risk	Mitigation
1	Payload container leak	Payload bay coated with fiberglass
2	Deployment mechanism malfunction	Multiple deployment mechanism trials
3	PADA System error	Manual override
4	Undetected obstacles by GTV	Algorithm testing and debugging
5	Landing gear defect	Impact assessment
6	Premature DAS termination	Repeated telemetry testing

Figure 1.2 List of Risks and Mitigation Actions

1.5 Discriminators

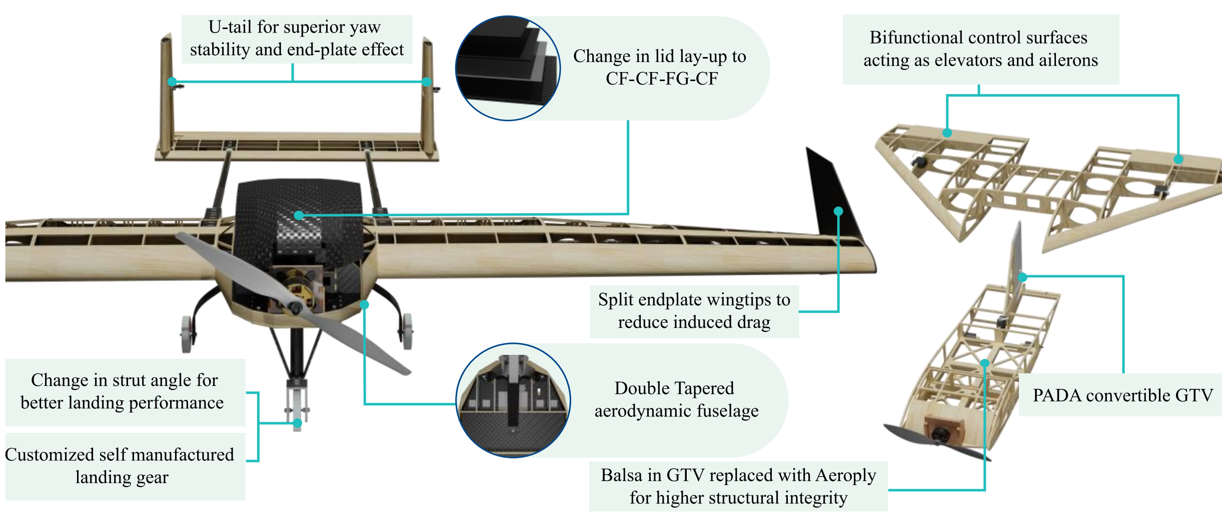

Figure 1.3 Exploded View of the System

1.6 Cost Breakdown

The team functioned according to a projected budget of $13,700 derived from an assessment of the inventory. It is segmented as depicted in the outer circle. Owing to sponsored equipment and university aid, we ultimately invested $12,000 as illustrated in the inner circle in *Figure 1.4.*

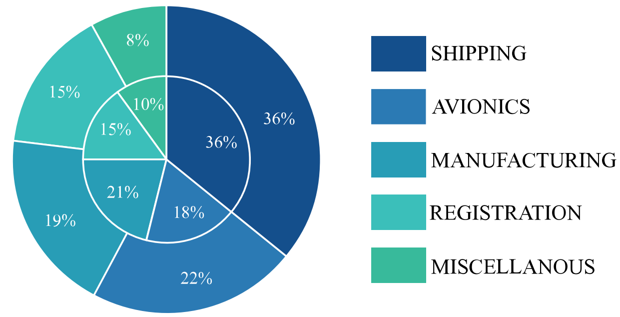

Figure 1.4 Expense Analysis

2. Schedule Summary

The Gantt chart provides a defined roadmap to pursue in order to attain the final objectives. By utilizing this visual tool, we adeptly managed our timeline by expediting delayed tasks.

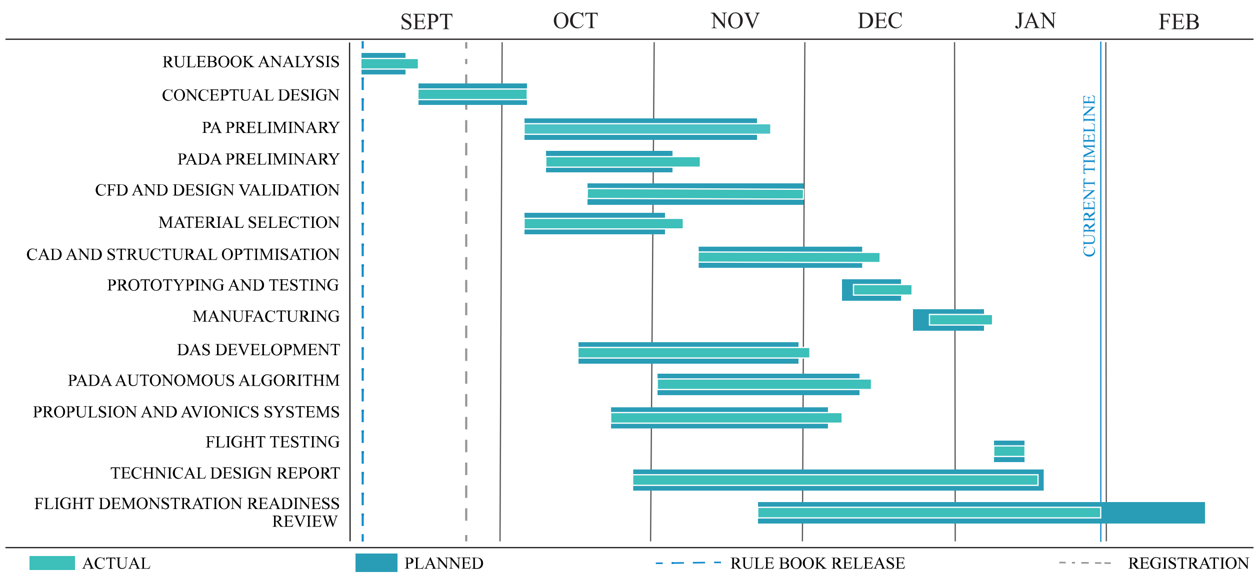

Figure 2.1 Gantt Chart

3. Environmental Considerations

The climatic conditions in Lakeland, Florida in March were taken into consideration to design the aircraft. Wind speeds consistently peak at 21 mph originating from the west with wind gusts up to 25 mph. These winds may also considerably impact the flight path of the aircraft, which necessitates the pilot to make frequent adjustments to maintain desired the trajectory. Calculations were made to accommodate any crosswinds with a 15% margin of error and the rudder was designed to assist the pilot during landing in such conditions.

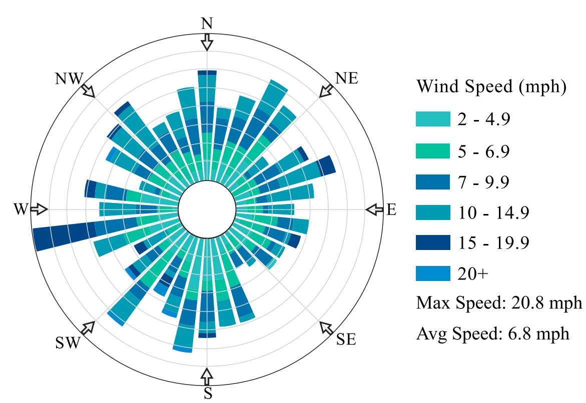

Figure 3.1 Wind Rose Chart

4. Design Specifications and Trades

4.1 Overall Design Layout and Sizing

Wing		Twin V-Stab		Elevator	
Airfoil	E421	Airfoil	NACA 0012	Span	36.22 in
Span	102.36 in	Span	13.39 in	Chord	5.35 in
MAC	22.84 in	MAC	11.42 in	Max Deflection	±25°
Taper Ratio	0.62	Taper Ratio	0.69	Area	193.75 in^2
Aspect Ratio	4.59	Root Chord	13.38 in	**Rudder**	
Area	2278.51 in^2	Area	310 in^2	Span	13.39 in
AoI	5°	Moment Arm	45.1 in	Chord	5.35 in
Fuselage		**H-Stab**		Max Deflection	±30°
Airfoil	GOE 390	Airfoil	NACA 0012	Area	71.67 in^2
Span	11.81 in	Span	36.22 in	**Aileron**	
MAC	35.83 in	Chord	13.39 in	Span	16.54 in
Taper Ratio	0.89	AoI	-3.5°	MAC	7.48 in
Aspect Ratio	0.33	Aspect Ratio	2.71	Max Deflection	±25°
Area	418.5 in^2	Area	485.15 in^2	Area	117.8 in^2

Table 4.1 Overall Design Layout and Sizing

4.2 Trade-Off Studies

4.2.1 Scoring Analysis

Through MATLAB, a Scoring Sensitivity Analysis was derived to predict optimized values of distance from the center of the landing zone (d) and $W_{payload}$. A 3D graph was plotted to compare flight score, d and $W_{payload}$. By adopting autonomous performance in GTV and random PADA zone multiplier (Z_{PADA}), the values in *Table 4.2* generated the best flight score and total score. Smaller values of d and higher values of $W_{payload}$ gave the highest flight score values. Ultimately, the results showed an ideal flight score of 32.49 when a water payload of 13.2 lbs was flown in each successful PA flight attempt.

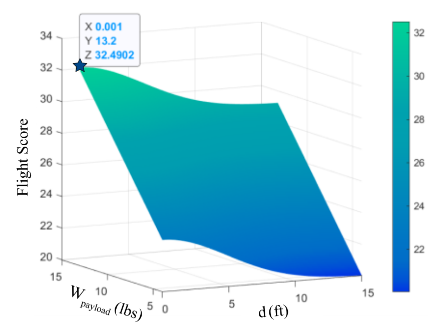

Figure 4.1 FS vs $W_{payload}$ vs d

Parameters		
$Z_{PADA} = 2$	$A_{GTV} = 5$	$\sigma = 4.87$
$W_{payload} = 13.2$ lbs		
$F.S = W_{payload} + 8*\left(Z_{PADA} + \left(5*\frac{1}{\sigma\sqrt{2\pi}}e^{\frac{-d^2}{2\sigma^2}}\right)\right)$		

Table 4.2 Scoring Analysis Parameters

4.2.2 Fuselage Configuration and Payload Placement

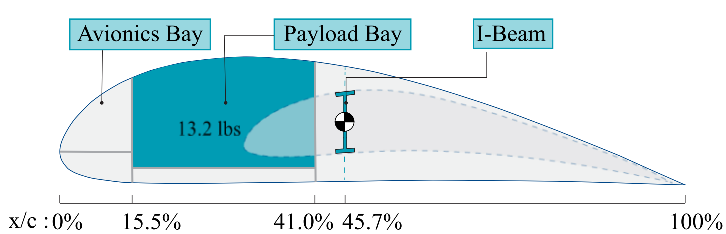

Figure 4.2 Chordwise Arrangement of Fuselage

An aerodynamic fuselage with a parabolic lateral cross-section was adopted. Plastic water bags were selected as the water-carrying mechanism for their lightweight, tearresistance and flexible dimensions. This achieved optimal Lift to Drag ratio (L/D) and maximum effective payload-bay volume with a packing efficiency of 84%, reducing form and interference drag. As shown in *Figure 4.2*, the bay positionings ensured a seamless wing-fuselage integration, maintaining the Center of Gravity (CG) coinciding with the wing's Aerodynamic Center (AC) to negate the moment due to lift.[7]

4.2.3 Wing Configuration

The monoplane design was selected as the decrease in weight and complexity outweighed the 12.5% higher L/D offered by the biplane design. The mid-wing configuration enabled aft placement of the wing, increasing payload bay volume. It ensured roll stability and minimized interference drag and structural weight in comparison to high and low wing configurations.[8]

Characteristics	Weightage	High Wing	Mid Wing	Low Wing
Aerodynamic Performance	30%	3	4	3
Structural Integrity	30%	3	4	2
Lateral Stability	20%	4	3	2
Ground Effect	20%	2	3	4
Total	100%	3	3.6	2.7

Table 4.3 Figure of Merit (FOM) Comparison for Wing Vertical Location (1-Least Favourable, 5-Most Favourable)

4.2.4 Wing Planform

A semi-tapered planform was selected for a 5.5% increase in L/D over a rectangular planform. It offered a shorter root chord than the tapered planform, decreasing structural weight and increasing payload volume. A Trailing Edge (TE) sweep was implemented to position the AC over the CG, reducing the load path and structural complexity.

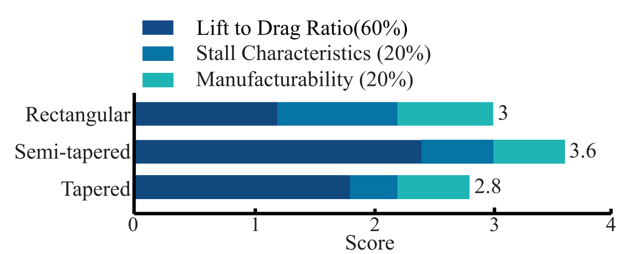

Figure 4.3 FOM Comparison for Planform

4.2.5 Tail Configuration

The U-tail's end-plate effect allows for a 15% smaller Horizontal Stabilizer (H-stab). This allows the Vertical Stabilizers (V-stab) to be sized to increase the yaw damping by 28% at a similar wetted surface area, which is crucial for the gusty weather conditions. In line with *Table 4.4*, the U-tail was finalized as it retains the modular structural design of the conventional tail.[2]

Characteristics	Weightage	T-tail	U- tail	Conventional
Stability and control	40%	4	4	3
Weight	30%	2	3	4
Wake Interference	15%	3	4	2
Manufacturability	15%	4	4	3
Total	100%	3	3.7	3.3

Table 4.4 FOM for Tail Configuration

4.2.6 Landing Gear Configuration

Trade-off assessment was done primarily based on weight distribution, on-ground stability and steering control. The tail dragger provided an advantage in propeller clearance but was dismissed for its susceptibility to crosswind landings at high crab angles. The tricycle allows for short field and 3-point landing, making it the ideal choice for the PA. The tricycle landing gear was designed for an overturn angle range of 25° to 63° ensuring stability even at the aft-most location of the CG without the static payload. [4]

Wheel Base	Wheel Track	Overturn Angle
21.22 in	24.21 in	61.73°

Table 4.5 Landing Gear Parameters

4.3 Design Features and Detail

4.3.1 Airfoil Selection

The team analyzed various airfoils within a range of Reynolds and Mach numbers based on the targeted mission requirement. The polars were thoroughly studied and a JAVA code was used to shortlist them based on specific characteristics showcased in *Table 4.6.* Airfoils for the wing and the fuselage were shortlisted for high-lift and volume requirements, respectively. Reflex airfoils were studied to design a longitudinally stable flying wing PADA, reducing airframe weight and maximizing payload volume.

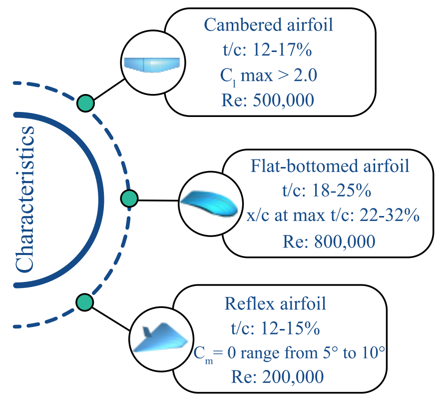

Figure 4.4 Criteria for Airfoil Selection

Wing Airfoil	α Stall (°)	C_L/C_{Dmax}	C_{Lmax}
FX74	11.5	118.54	2.16
E421	14.5	107.92	2.04
E423	12.5	123.74	2.03

Fuselage Airfoil	x/c (%)	C_L/C_{Dmax}	t/c_{max}
GOE 390	28.82	96.84	20.32
GOE 382	30.92	100.44	20.02
GU25-5(11)8	41.14	121.4	20.01

PADA Airfoil	C_m avg	C_L/C_{Dmax}	t/c_{max}
E325	0.03	8.64	12.63
E326	0.02	8.65	12.87
E355	0.01	8.54	12.59

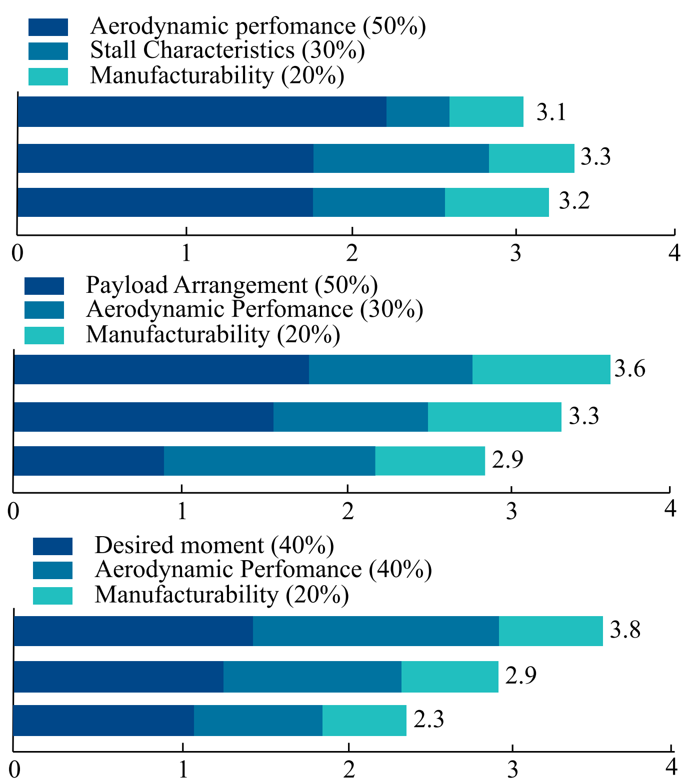

Table 4.6 Airfoil Characteristics (left) and FOM Comparison (right)

4.3.2 Wing Sizing

The wingspan was set at 102.36-inch, with a 15.75-inch fuselage span and a 1.89-inch tolerance left for manufacturing and winglet integration. To identify the optimal power and wing loading, constraint analysis was conducted with Aspect Ratio (AR) coupled along with planform area, The design point was found for maximizing the allowable take-off weight, while meeting the performance requirements for take-off, climb gradient, stall velocity and sustained turn, as set by the competition flight plan. The root chord, taper ratio, and taper start were fine-tuned and then the design with the highest $C_L^{3/2}/C_D$ was selected for prioritizing endurance over range.

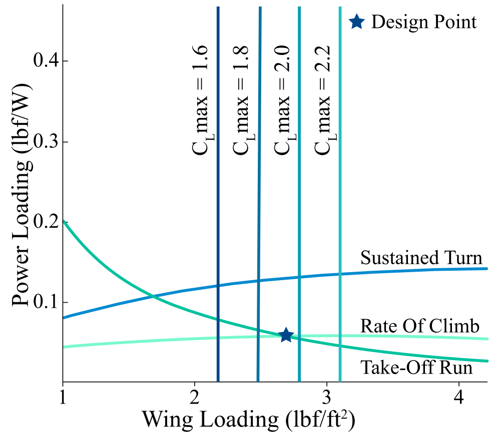

Figure 4.5 Constraint Analysis

Stall Speed	Take-off weight	$C_L^{3/2}/C_D$
30.6 ft/s	42.49 lbf	9.76

Table 4.7 Initial Wing Approximations

4.3.3 Fuselage Sizing

The team determined the minimum chord of the fuselage to accommodate the PA avionics and wing integration structures while maximizing payload bay volume. Computer Aided Design (CAD) modelling of the water packs and Computational Fluid Dynamics (CFD) analysis was conducted to achieve optimal effective payload volume and wing-fuselage L/D. As shown in Figure 4.6 the root chord was varied and the design point was identified. A 3.97-inch fairing was incorporated in the design to facilitate a smooth transition of flow at the wing-fuselage junction.

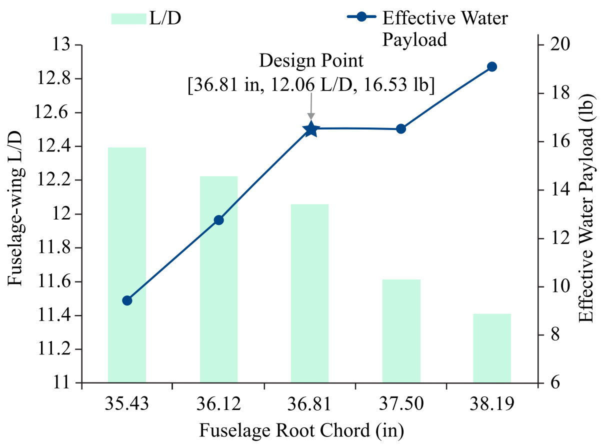

Figure 4.6 Fuselage Optimization Graph

4.3.4 Tail Sizing

The NACA 0012 airfoil was chosen for the PA's tail surfaces due to its ideal thickness, which increases structural durability and allows for servo placement. The selected 40.28-inch moment arm achieves stability derivatives within ranges specified in *Table*

Parameter	Range	Value
V_V	0.02 to 0.12	0.042
V_H	0.2 to 1.1	0.31
Static Margin	10% to 15%	14.1%
Cm_0	≥0	0.0007
Cm_q	-5 to -40	-7.124
Cn_β	≥0.1	0.1003
Cn_r	-0.1 to 0.1	-0.092

Table 4.8 Tail Sizing Conventional Ranges

4.8, while minimizing the wetted surface area and boom flexure. Equal root chords were used for the horizontal and twin vertical stabilizers to increase manufacturing ease. A thorough validation of the design was conducted using XFLR5, AVL, and CFD analyses.[5]

4.3.5 Control Surface Sizing

The control surfaces of the PA were sized according to specifications of aircraft class I, flight phase B and level of acceptability 1.[4]

Take-off pitch angular acceleration	12°/s²
Required spin recovery rate	80.21°/s²
Time required to bank 45°	1.7s

Table 4.9 Control Surface Requirements

Rudder Sizing

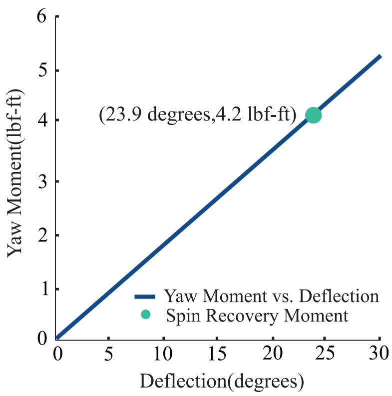

Figure 4.7 Deflection vs Yaw Moment

The rudder sizing was done alongside the V-stab design, to satisfy the crosswind landing conditions, and the design with the least crab angle at 30° deflection was finalized. The team developed a MATLAB code utilizing anti-spin moments of inertia to ensure that the selected rudder could recover the plane from a spin at 45° Angle of Attack (AoA) within the set maximum deflection of 30°.

Elevator Sizing

An elevator with chord ratio of 40% corresponding to an AoA effectiveness of 60% was designed to achieve a take-off rotation angular acceleration of 10°/s^2 at the maximum deflection of 25°. The team developed a MATLAB code to ensure longitudinal trim at varied speeds in the flight envelope.

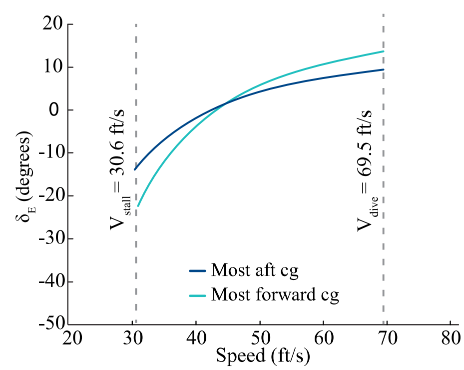

Figure 4.8 Deflection vs Speed for Level Flight

Aileron Sizing

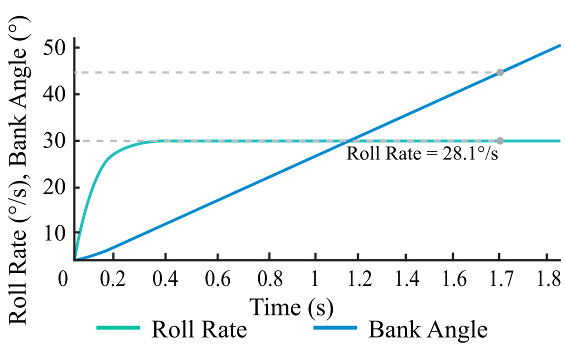

Figure 4.9 Time vs Roll Rate & Bank Angle

The ailerons placed at 95% outboard position of wingspan with maximum deflection of 25° reduces the effect of wingtip vortices, allay stalling risk and maximize roll control with a maximum structurally viable chord length for maximum roll moment arm. They were sized to achieve a 45° bank angle in 1.7s at maximum deflection for the aircraft class and the critical take-off regime.[6]

4.3.6 Servo Sizing

The control surfaces of the PA were analysed through CFD simulations at maximum deflection with a dive airspeed of 69.5 ft/s using their respective control rod, control horn and actuator arm to determine the greatest hinge moment due to aerodynamic forces. A factor of safety (FOS) between 1.2-1.6 was applied, to accommodate for torque reduction due to frictional forces.

Control Surface	Number of Servos	Hinge Moment (oz-in)	Selected Servo	Torque Required per servo(oz-in)	Total Available per Servo (oz-in)	FOS
Aileron	2 each	230.34	Hitec HS-5645MG	133.03	168.03	1.27
Elevator	2	106.20	Hitec D-625MW	83.32	122.20	1.47
Rudder	1 each	22.6	Hitec HS-5496MH	55.54	83.32	1.5

Table 4.10 Servo Selection

4.4 Design Optimization

4.4.1 Wingtip Devices

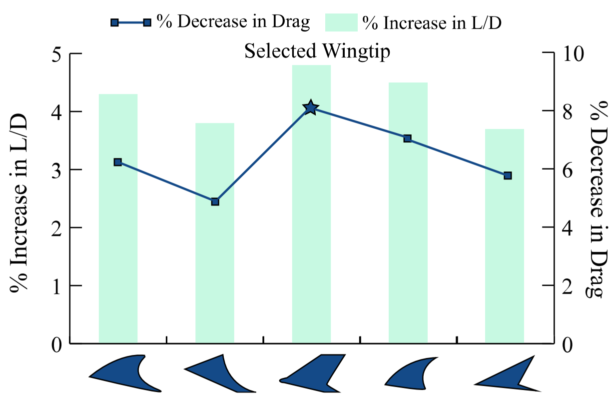

Figure 4.10 Comparison of Wingtip Devices

Wingtip devices design was done by parameterised variation of height above and below the chord, taper ratio, and placement of known endplates to optimize L/D due to the endplate effect. Among the five best performing options shown in *Figure 4.10*, the forward wingtip fence using a flat plate offered the highest L/D improvement. The increased parasitic drag was countered by significant reduction in induced drag.

4.5 Stability

4.5.1 Static Stability Analysis

The negative and positive slopes in *Figure 4.11* depict longitudinal and directional static stability, respectively for the PA and PADA with optimal static margins. The trim angles are 0.1° and 0.4° for PA and PADA, respectively, at their corresponding cruise velocities.[3]

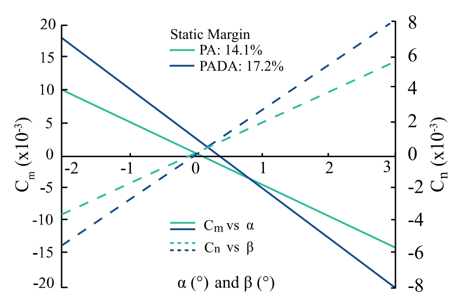

Figure 4.11 Static Stability of PA and PADA

4.5.2 Dynamic Stability Analysis

Characteristic	Longitudinal Modes		Lateral Modes		
	Short Period	Phugoid	Dutch Roll	Roll	Spiral
Eigen Values	-2.10 ± 5.53i	-0.02 ± 0.82i	-2.10 ± 5.53i	-7.83	0.29
Natural Frequency (Hz)	2.40	0.14	0.81	-	-
Damping Ratio	0.98	0.06	0.42	-	-

Table 4.11 Dynamic Stability Values

The eigenvalues and stability levels for longitudinal and lateral modes were computed using AVL. All modes, apart from the spiral mode, exhibited Level I acceptability prior to and following the release of PADA. A sufficient time-to-double of the spiral mode gives the pilot sufficient time for corrective actions.[5]

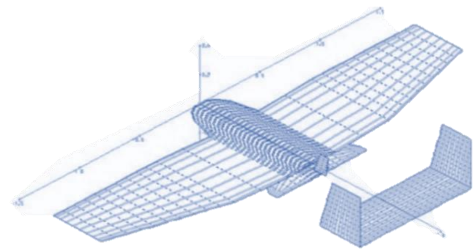

Figure 4.12 Aircraft Geometry

4.6 Powered Autonomous Delivery Aircraft Design

The PADA was crafted for optimal stability and landing performance, minimizing structural damage and successfully landing within a minute after deployment. Keeping in mind the objectives and constraints, two iterations were compared, as outlined in *Table 4.12*. The cropped delta wing was selected in lieu of its superior stall angle of 16°, attributed to the development of LE vortex, and its lower induced drag. In consideration of the PADA placement and a 16 oz weight limit, the team defined limits for chord and span as 23.62 and 29.53 inches, respectively. To enhance control and minimize weight within structural limits, the design underwent optimization by varying the taper ratio from 0.25-0.5, with a minimum tip chord of 1.57 inch to maintain manufacturing feasibility. At an AoA of 5°, the wing demonstrated the highest L/D of while satisfying the lift requirements for carrying 7.34 oz of payload.[1]

Wing		V-Stab		Elevon	
Airfoil	E325	Airfoil	Flat Plate	Span	7.09 in
Span	29.53 in	Span	5.14 in	Chord	2.78 in
Root Chord	19.68 in	Root Chord	5.83 in	Deflection	± 30°
Tip Chord	5.51 in	Tip Chord	4.08 in	**Rudder**	
Taper Ratio	0.28	Taper Ratio	0.7	Span	5.14 in
Aspect Ratio	2.11	Area	25.48 in²	Chord	4.08 in
AOA	5°	Tail Arm	8.2 in	Deflection	± 30°

Table 4.12 PADA Design Layout and Sizing

Configuration		Weight	Aerodynamics
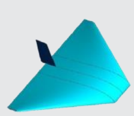	Cropped delta wing with single V-stab	15.83 oz	Reduce wingtip vortices hence reducing induced drag resulting in higher L/D
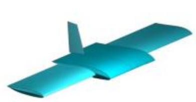	Rectangular wing with airfoil shaped fuselage and single V-stab	16.35 oz	Higher interference drag which reduces L/D

Table 4.13 Comparison of PADA Iterations

5. Analysis

5.1 Software Analysis and Testing

5.1.1 Data Acquisition System

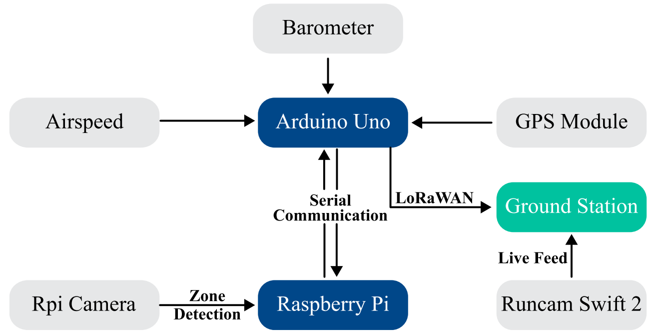

Figure 5.1 Communication Systems Interface

The aircraft's Data Acquisition System (DAS) was developed after careful consideration of competition requirements, encompassing factors such as data processing latency and display functionality. The meticulous selection of sensors, namely the MS-5637 Barometric Pressure Sensor and the MPXV7002DP Airspeed Sensor, entailed comprehensive research and a detailed examination of individual data sheets. A pivotal consideration was ensuring their compatibility with the Arduino Uno microcontroller, to which they are intricately linked. To enable live video feed from the aircraft, the Runcam Swift 2 is used and a 16 Mega Pixel Universal Serial Bus (USB) camera is employed for circle detection. A RaspberryPi (Rpi) 5 board with a 1000mAh battery pack is used to run the zone detection algorithm. During the circle detection process, once the required circle is identified, an alert of detection, along with the timestamp, is transmitted to the Arduino board. The Arduino, serially connected to the RPi, in conjunction with the Ublox NEO-6M, acquires GPS coordinates. The data collected from all the sensors is then transmitted to the ground station to display in the DAS via the Long-Range Wide Area Network (LoRaWAN) communication protocol.

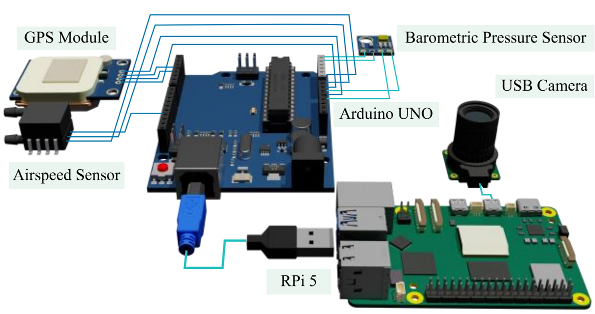

Figure 5.2 Sensors Interface

Graphical User Interface (GUI)

The GUI delivers live visualization of critical in-flight data, including altitude, airspeed, flight time and waypoint coordinates, while also indicating PADA deployment status. The deployment zone colors and coordinates are showcased and visualized on a map, in sync with the real-time flight trajectory. The GUI integrates a live camera feed from the PA.

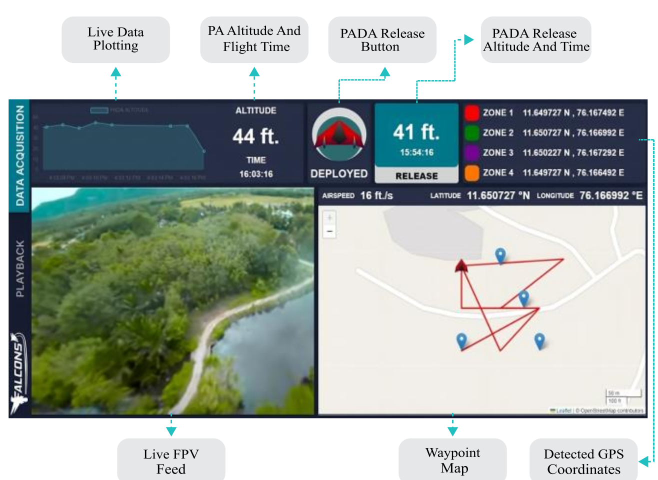

Figure 5.3 DAS User-Interface

All data is simultaneously stored for instant on-demand access, offering a concise and comprehensive solution for monitoring and post-flight analysis.

Testing

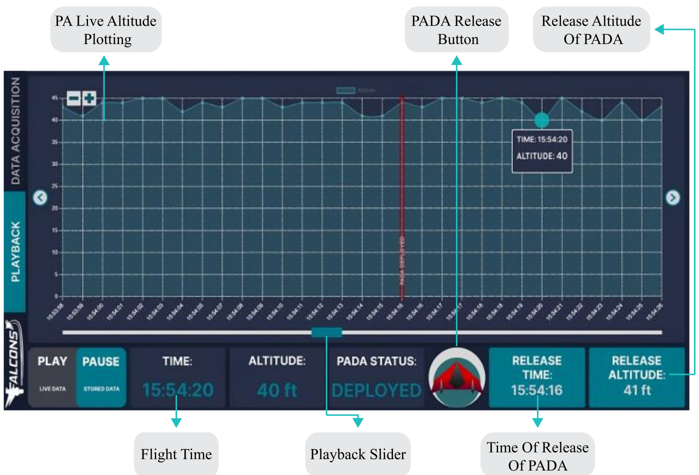

Figure 5.4 Live Plotting of Altitude Data

The DAS underwent a thorough testing procedure using a drone, with each test specifically designed to provoke failures in the system. While testing, special attention was given to ensuring the functionality of the Playback button window. This involved assessing the operation of the Playback Button, displaying the PADA release status, and presenting various details such as the altitude of the PA and the release altitude of PADA, along with additional information. Test results from a drone helped identify potential failure points in the DAS, leading to the implementation of necessary precautions and upgrades to prevent failures during actual flights. To ascertain the accuracy of the GPS module, it was compared with values obtained from Google Maps. Testing showed that the Barometric Pressure sensor was 96% accurate in the range of 25 to 45 ft.

Figure 5.5 DAS Testing

5.1.2 Guided Landing System

The automated functionalities of the PADA are enabled through integration with the Kakute F4 Mini flight controller, which interfaces with a receiver module and a GPS module. The GPS coordinates, obtained from the avionics of the PA are relayed through the ground station to the PADA. The interfaced receiver module helps in receiving the data that the ground station is transmitting.

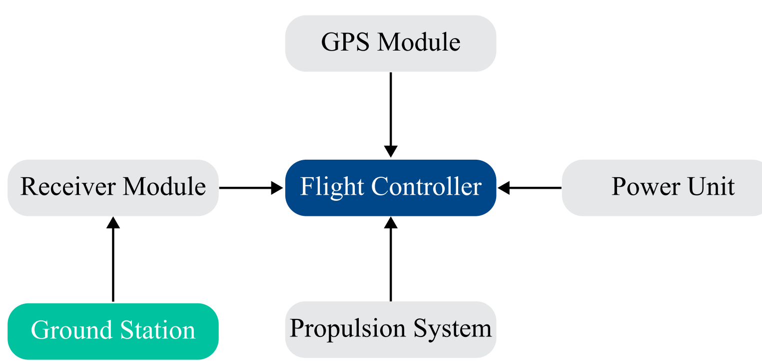

Figure 5.6 PADA Avionics System

5.1.3 Adaptive Zone Detection and Navigation

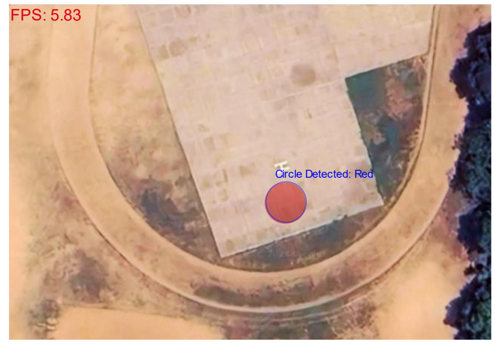

Figure 5.7 Circle Detection at an Altitude

The Adaptive Zone Detection and Navigation algorithm derives its inspiration from the Hough Transform, specifically incorporating Pixel Analysis for circular shapes. This innovative approach meticulously analyzes image pixels, identifying circular shapes by transforming them into a parameter space (C: x, y, r). By leveraging the robust principles of the Hough Transform and integrating proprietary adjustments, it ensures generation of precise landing zones. The decision to use this algorithm over alternatives is grounded in its unique balance between accuracy and adaptability. Unlike certain machine learning models and other algorithms, this approach doesn't prerequisite extensive training data, enabling precise and dynamic circle detection.

5.1.4 GTV Routing

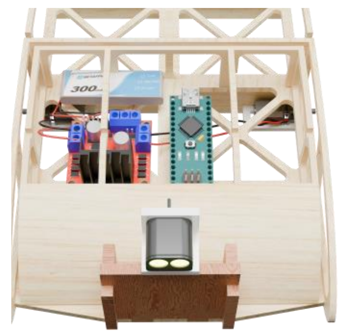

Figure 5.8 Hardware Integration in GTV

The GTV operates autonomously with the TF Luna LiDAR sensor mounted on a servo, interfaced with an Arduino Nano. It is driven by an L293D motor driver, enabling it to be a 4-wheel drive. It is steered differentially to achieve an optimum turn radius.

Dynamic Vector Mapping

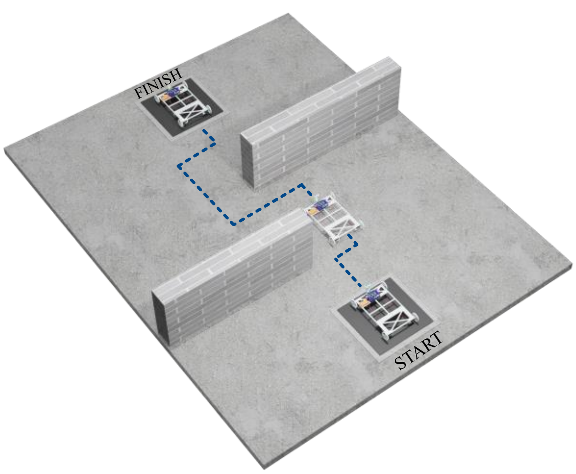

Figure 5.9 Ideal GTV Routing

For navigation, the Dynamic Vector Mapping (DVM) algorithm was developed based on a refined combination of Simultaneous Localization and Mapping (SLAM) , which was subsequently tailored to meet our specific requirements. SLAM uses sensor data to create a grid-based map, updating the GTV's position with respect to obstacles which are detected dynamically. The Potential Field method guides the GTV using attractive forces towards the goal and repulsive forces to avoid obstacles. During the development of DVM, the A* algorithm was also considered. A* finds the shortest path in a grid-based environment by marking obstacles as blocked cells and determining the path using a cost function. After evaluation in an environment simulating the competition, A* is found effective in pre-defined environments but may reroute when new obstacles are detected, causing delays. SLAM uses the potential field method to dynamically update obstacle positions, offering more accurate and timely navigation. Hence, DVM was developed after a careful examination of the accuracy of both the algorithms in the scenario presented by the competition. The effectiveness of DVM was validated after physical testing as it proved 25% more effective than the A* algorithm.

5.2 Design Evaluation and Performance Analysis

5.2.1 Computational Fluid Dynamics

Steady state computations were done in a turbulent viscous regime, using an incompressible flow solver involving RANS equations in STAR-CCM+ to optimize aerodynamic performance. The K omega-SST turbulence model was applied to an optimized mesh in the wake and boundary region of the PA to additionally analyze the induced drag. The aircraft achieved a total lift of 35.423 lbf and drag of 3.826 lbf.

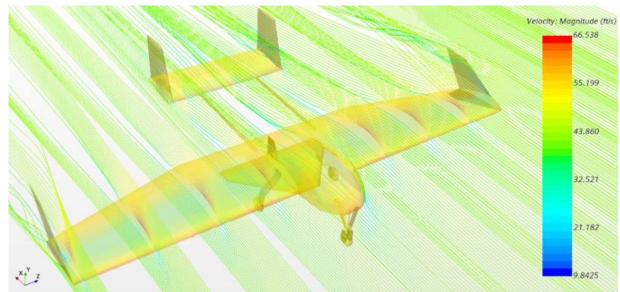

Figure 5.10 Full Body CFD

5.2.2 Stall Analysis

The stall characteristics of the PA were investigated by analyzing the streamlines and lift profile of the aircraft within a range of 16° to 24° AoA based on the 2D lift curve, at cruise velocity. A substantial change in flow behavior and L/D became evident at 19° AoA.

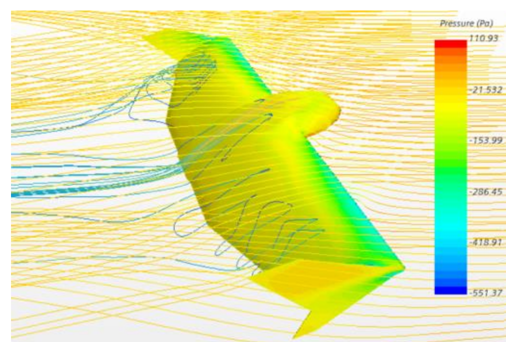

Figure 5.11 PA Stall Analysis

5.2.3 Lifting Performance

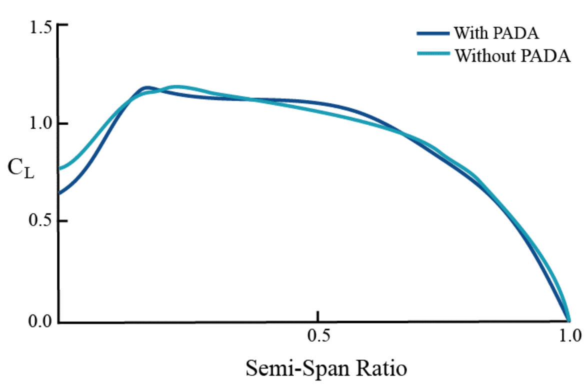

Figure 5.12 Lift Distribution Curve

To estimate the effect on the lifting performance of the PA before and after the release of the PADA, lift distribution curves were plotted at cruise velocity using AVL. A negligible change in the lifting performance was observed, ensuring the unhindered operability of the aircraft post release of the PADA.

5.2.4 Drag Analysis

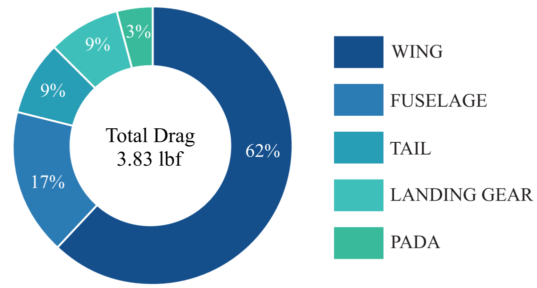

Figure 5.13 Drag Breakdown

Figure 5.13 illustrates drag contributions from components of the PA at cruise speed, as determined through CFD analysis. With the wing and fuselage being primary contributors, wingtip devices and fairings between them were implemented to minimize induced and interference drag. Through a systems design approach, an optimized PADA design was achieved adding negligible overall drag.

5.2.5 Aeroelasticity

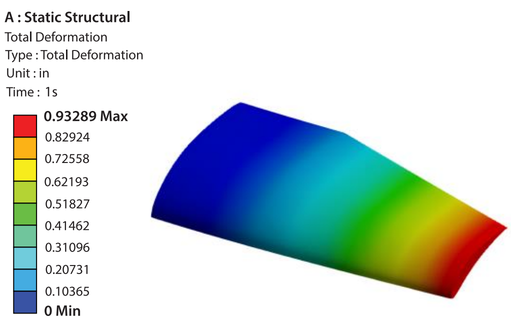

Figure 5.14 Aeroelasticity

Surface mapped pressure data of ribbed-wing in ANSYS FLUENT showed stress formation due to aerodynamic load with a maximum deflection of 0.93-inch near the wingtips. This deflection by the use of CF spars yields a dihedral angle, enhancing lateral stability.

5.2.6 Take-off and Landing Performance

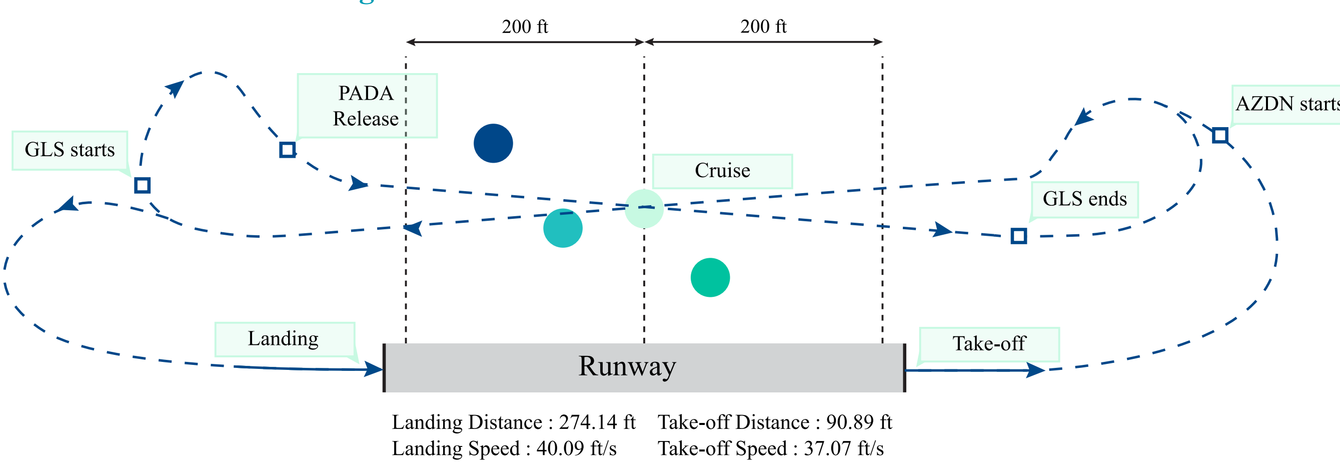

Figure 5.15 Flight Path and Performance

5.2.7 Flight and Maneuver Performance

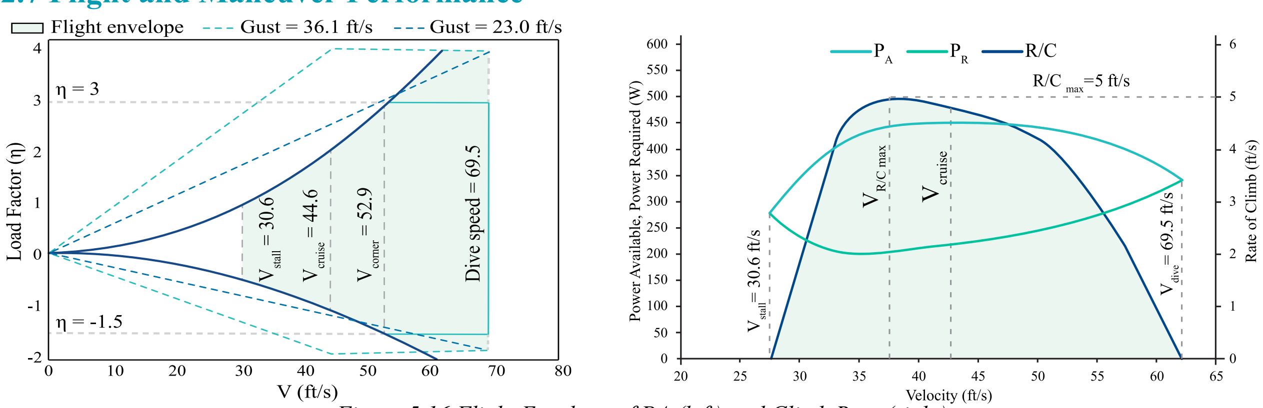

Figure 5.16 Flight Envelope of PA (left) and Climb Rate (right)

Through aeroelastic and structural analysis, the weakest components set positive and negative limit load factors at 3 and -1.5 in the flight envelope, defining a corner velocity of 52.9 ft/s. This ensures excellent turn performance close to cruise speed. Ansys was used to verify structural viability with a safety factor of 2.6 when extending the envelope, to factor in gust lines. A Rate of climb (R/C) of 4.8 ft/s was attained at cruise velocity. Figure 5.16 shows the key performance parameters of the PA.[3]

5.3 Structural Analysis

Component	Wing Rib 	Spar 	Wheel 	Nose Gear 	Landing Gear 	Empennage 
Max Stress(MPa)	9.07	225.66	26.1	441.50	257.44	344.13
Desired FOS	1.10	2.53	1.5	1.27	2.01	1.45
Realized FOS	1.14	2.66	1.53	1.35	2.33	1.74
Critical Margin	0.05	0.16	0.03	0.08	0.33	0.29

Table 5.1 Critical Margins

5.3.1 Applied Loads

Rib

Truss	No truss	Bowstring-Warren	K-Bowstring	Modified K	Bowstring-K
Aggregate Mass (lb)	0.88	0.54	0.54	0.53	0.53
Deformation (in)	0.09	0.21	0.24	0.20	0.22
Max Stress (MPa)	5.94	9.06	9.99	9.06	9.94
FOS	1.75	1.15	1.04	1.15	1.04

Table 5.2 Truss Comparison

Balsa was chosen for wing ribs for its excellent strength-to-weight ratio. ANSYS Static Structural analysis was performed, applying aerodynamic pressure gradient at a 5° incline. The desired Factor of Safety (FOS) of 1.1 safeguards the structural integrity against unanticipated loading contingencies. The Modified K trussed rib of 0.16-inch thickness was chosen for its efficient load distribution, making it optimal for counteracting the shear forces experienced.

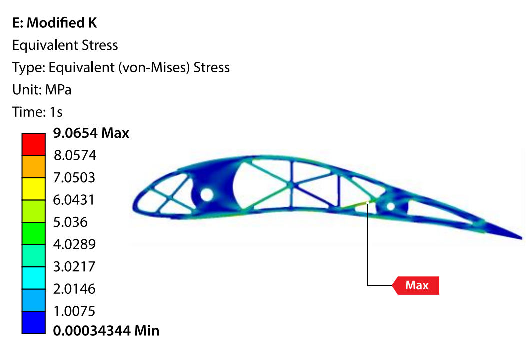

Figure 5.17 Truss Analysis

Spar

To ensure wing integrity in variable wind conditions, ANSYS Static Structural analyses was performed on the telescoped spars of optimized diameter considering maximum aileron deflection and stall AoA as

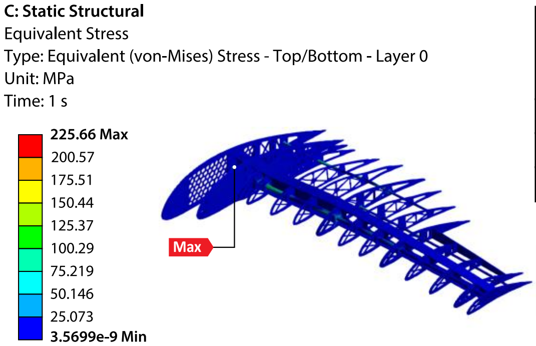

Figure 5.18 Spar Analysis

Primary Spar OD Configuration (in)	Mass (lb)	Deformation (in)	Deflection (°)	Max Stress (MPa)	FOS
0.55-0.63	0.56	2.12	2.23	302.23	1.96
0.63-0.71	0.64	1.54	1.52	272.35	2.38
0.71-0.79	0.73	1.04	1.01	252.66	2.66

Table 5.3 Spar Analysis

20°. For a desired FOS of 2.5, the tri-spar configuration was selected for its ability to withstand bending stresses and torsional strain. It consists of two 3K twill weave tubes with Outer Diameter (OD) of 0.79 and 0.71-inch as well as an I-beam with a web thickness of 0.24-inch and a flange thickness of 0.16-inch.

Wheel

Spoke	 4-Spoke	 5-Spoke	 6-Spoke
Mass (lb)	0.16	0.16	0.16
Deformation (in)	0.29	0.26	0.21
Max Stress (MPa)	33.52	26.15	29.66
FOS	1.24	1.58	1.41

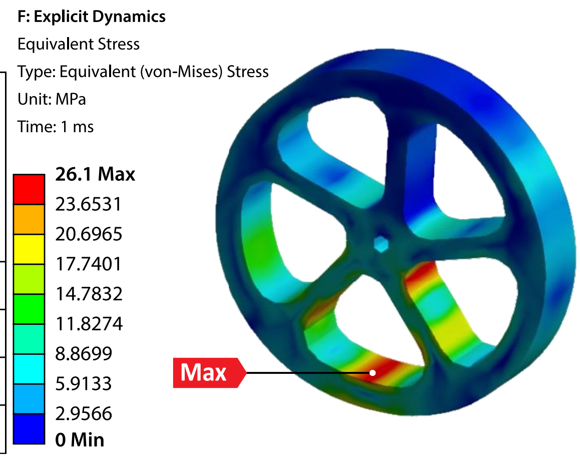

Figure 5.19 Spoke Comparison (left) and Wheel Analysis (right)

The wheel was designed to withstand 200 N of load applied by the PA while landing using Polylactic acid (PLA) in the additive manufacturing process for its lightweight durability, adaptability and minimal frictional characteristics. ANSYS Explicit Dynamics analysis was performed, during which the wheel was drop tested from an elevation of 13.12 ft. onto a concrete floor, with a desired FOS of 1.5 to combat the touchdown forces. A 5-spoke wheel having a diameter of 3.94-inch and 0.71-inch thickness was chosen to resist the high-frequency vibrations. Multiple drop tests were performed on the manufactured wheel from a height of 25 ft to check the endurance.

Nose Landing Gear

Shape	Mass (lb)	Deformation (in)	Max Stress (MPa)	FOS
U	0.70	0.15	1006.78	0.59
V	0.77	0.09	525.34	1.19
Broad-V	0.78	0.08	441.50	1.35

Table 5.4 NLG Shape Comparison

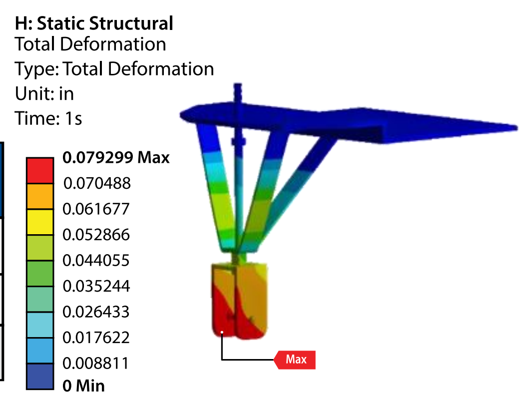

Figure 5.20 Nose Landing Gear

The PA was designed with a tri-cycle configuration consisting of the Main Landing Gear (MLG) and Nose Landing Gear (NLG), which enhances the on-ground directional control and eliminates the risk of nose tipping. To optimize the safe load upon touchdown, the NLG is composed of specially designed 3K Twill CF struts combined with a Stainless-Steel fork and an Aluminium 1060 alloy rod featuring a mild steel insert. Using ANSYS Static Structural analyses, struts of different configurations were iterated by applying force on the axle hole. A broad V-strut was chosen to minimize wobbling and is 1.18-inch wide and 0.118-inch thick. The desired FOS of 1.27 promotes baseplate stabilization. As a result, the front V-strut seamlessly distributes the load across the avionics baseplate while the rear half of the V-strut provides supplementary posterior support along the payload baseplate.

Main Landing Gear

Shape	Straight 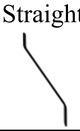	Curved 	Concave 
Mass (lb)	0.382	0.404	0.454
Max Stress (MPa)	282.28	257.44	277.1
FOS	2.126	2.33	2.17

Table 5.5 Main Landing Gear Comparison

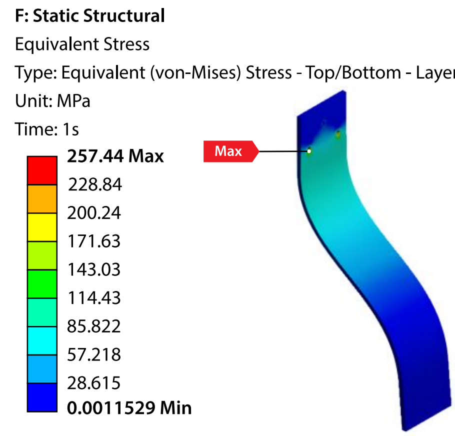

Figure 5.21 Main Landing Gear

To withstand the touchdown forces of the PA, a custom MLG was engineered using 3K Twill CF (200 GSM) for its load-bearing capacity in dual planes. It was cycled through ANSYS Composite PrepPost to test its resilience against landing forces, which was determined to be 80% of the PA weight. S-struts of 2.36-inch wide and 0.2-inch thick were chosen as it efficiently resisted the shear and torsional forces on impact. The desired FOS of 2 considers the fatigue due to repeated landings and the sharp loads borne by the struts on touchdown.

Empennage

Configuration	Mass	Deformation	Max Stress	FOS
Twin Boom 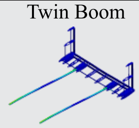	2.16 lb	3.58 in	344.13 MPa	1.74
Single Boom 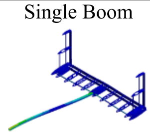	1.92 lb	5.42 in	476.15 MPa	1.26

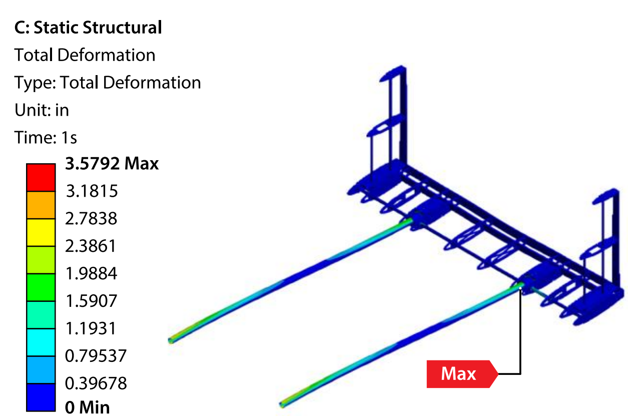

Figure 5.22 Boom Configuration Comparison (left) Tail Analysis (right)

ANSYS Static Structural analyses was performed for the empennage with different boom configurations, projecting lift data on the H-stab to test maximum flutter and torsion under extreme headwind conditions. The boom is made of 3K Twill CF of a 0.87-inch OD spar to withstand buffeting. For a desired FOS of 1.45, the twin cylindrical boom configuration was selected to counteract the dynamic loads and bending moments ensuring stability in turbulent winds.

5.3.2 Mass Properties and Balance

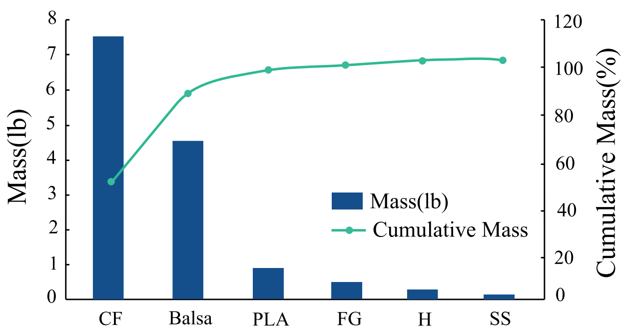

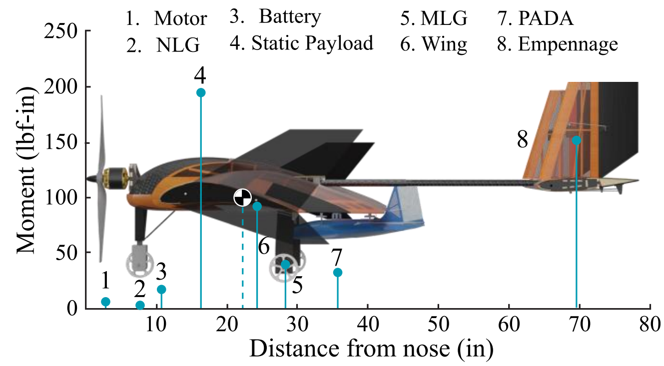

Figure 5.23 Cumulative Pareto Diagram (left) and Moment Balance Diagram (right)

6. Assembly, Subassembly and Integration

6.1 Fuselage

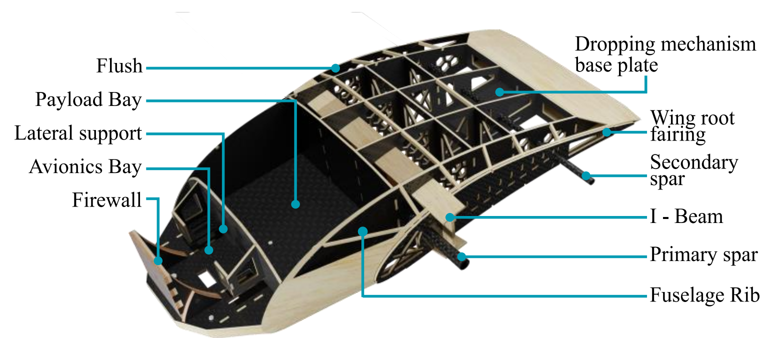

Figure 6.1 Fuselage Components

The structure primarily consists of ribs, baseplates, wing root fairings and lateral supports joined together using mortise and tenon joineries. The weight of these members is optimized by blanking and trussing. The composite end ribs (CF-FG-B-FG-CF) counter the loads transferred by the wing, force induced by lift and the impact on landing. The avionics baseplate bears the load of the avionics system along with the NLG and the force generated by the motor's thrust transferred through the firewall (FG-B-P-FG) while the payload baseplate bears the load of the static water payload. A third baseplate houses the 3D-printed PLA rotor and key dropping mechanism to release the PADA from the PA. To reinforce against transverse loads, the baseplates are composed of a Nomex core (CF-FG-HC-FG-CF). The avionics bay and payload bay are separated by the lateral supports (CF-FG-B-FG-CF). The avionics and payload bay are protected from Foreign Object Damage (FOD) by a composite lid (CF-FG-CF). Starting from the fuselage, Ultrakote has been applied on the PA to maintain the aerodynamic contour while minimizing added weight.

6.2 Wing

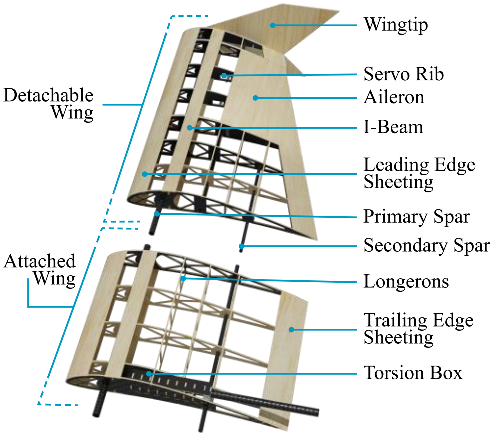

Figure 6.2 Wing Components

The wing is bifurcated into two distinct sections. The fixed section accounts for 35% of the wing, attached to the detachable segment with a telescoping mechanism that is locked in place by ball lock pins, improving the portability of the aircraft. The I-beam placed at the AC restrains wing flexure along its length, whereas the primary and secondary spars of OD 0.79-inch and 0.47-inch respectively resist the torsional moment experienced by the wing. The end and servo ribs of both sections consist of (CF-CF-B-CF-CF) composition to impart rigidity under dynamic loads. A 0.08-inch thick balsa sheeting is affixed to the LE and TE with longerons, ensuring structural support for the skin while maintaining the airfoil contour. The LE sheeting is supported by a 0.24-inch longeron at the front edge. A complete balsa aileron was made with ribs attached to a 0.16-inch thick slotted panel to assist with assembly and provide a template for the ribs.

6.3 Empennage

A twin CF boom with an OD of 0.79-inch uses a telescopic arrangement to further aid in the portability of the aircraft. It is secured to the wing on one end and to the H-Stab on the other using torsion boxes. The H-Stab uses a CF spar of OD 0.47-inch that is segmented into three sections to accommodate the boom and is secured to the torsion box with the help of a PLA nexus. For rear support, a 0.23-inch thick balsa beam and frame was incorporated across the H-stab to aid in the alignment of ribs. The V-stab consists of three composite ribs (CF-B-CF), positioned across a 0.31-inch OD CF spar. V-stab integration utilizes an Extruded Polystyrene foam block sandwiched between (CF-B-CF) plates in the H-Stab, with holes for V-Stab spar insertion and two M4 screws securing the bottom rib on either V-Stab.

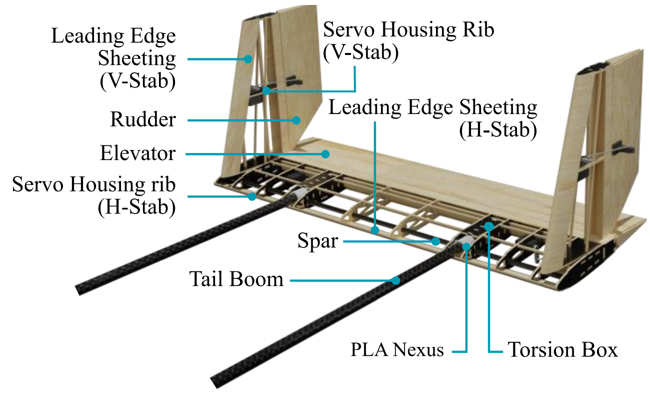

Figure 6.3 Empennage Components

6.4 Powered Autonomous Delivery Aircraft

The PADA utilises a detachable wing, simplifying the conversion to a GTV, which shortens assembly time and further supports the payload bay's volume expansion. 0.2-inch plywood is used for the firewall and its supports, which help resist wake. Aeroply of 0.11-inch thickness was introduced to enhance the airworthiness while minimising weight by blanking components such as end ribs and the payload baseplate. The V-stab extends from a dorsal fin, secured by a dove-tail joinery onto the empennage rib interlocked to the rear bulkhead. The wing section of this iteration is composed of 0.15-inch thick balsa also used for the ribs, elevons, and lateral supports that fasten onto the GTV component while serving as a payload lid through balsa longerons. Two ABS keys at the front and aft positions lock onto the dropping mechanism beneath the fuselage.

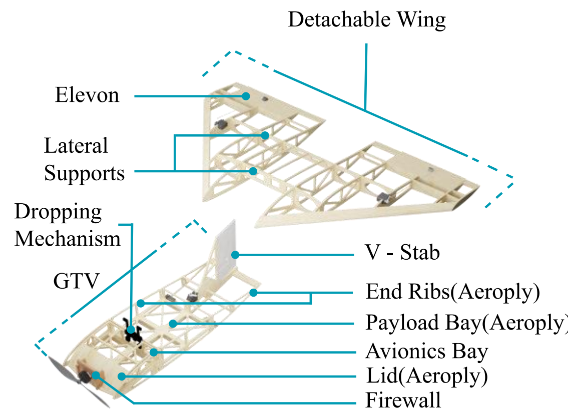

Figure 6.4 PADA and GTV Components

6.5 Ground Transport Vehicle

The quick turnaround time for the GTV is ensured by the removable section of the PADA-Convertible iteration. The Aeroply lid secures the dedicated electronics bay, ensuring components remain stable during operation, while the Aeroply motor-supports secure the attachment for wheel motors. To carry water, Polyethylene-low density bags were chosen for their high efficiency and are secured in the payload bay by the end ribs and bulkheads. The PADA-Convertible iteration was chosen for its ample payload capacity and effective utilization of a structure that can be repurposed as a GTV.

Description	X-iteration GTV 	Convertible GTV 	Foldable GTV 
Chasis structure	Collapsible ABS scissor structure with increased base support	PADA-GTV detachable with a designated payload area	Foldable ABS plate providing larger surface area
Drive mechanism	4-wheel differential drive	4-wheel differential drive	2-wheel differential drive
Chasis weight	0.26 lbs	0.25 lbs	0.39 lbs
Water capacity	24.70-32.94 oz	27.43-35.27 oz	29.56-37.66 oz

Table 6.1 Comparison of GTV Iterations

7. Powerplant Selection

7.1 Primary Aircraft

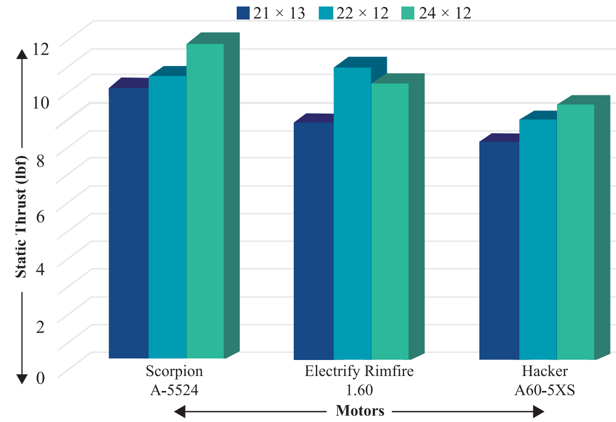

Figure 7.1 PA TMD Results

The team utilized eCalc software to opt for an appropriate motor-propeller setup. To refine the selection, a custom algorithm was developed. This program systematically cycled through all combinations of available motors, propellers, Electronic Speed Controllers (ESC) and batteries factoring in Revolutions Per Minute (RPM), static and dynamic thrust. The objective was to attain a thrust-to-weight ratio within 0.26-0.35. Durability and strength were weighed in for propeller choice. Subsequent to validation using a Thrust Measuring Device (TMD), the Scorpion A-5524-205Kv paired with a 24x12E propeller emerged as the final choice. The PA was powered by a Turnigy 5000mAh 6S 45C Li-Po battery, a 100A ESC, and a 750 W NeuMotors Power limiter.

Motor Selected	Kv	Static Thrust (lbf)	RPM	Propeller
Scorpion A-5524	205	10.84	3671	APC 24×12E

Table 7.1 Characteristics of Selected PA Powerplant

7.2 Powered Autonomous Delivery Aircraft

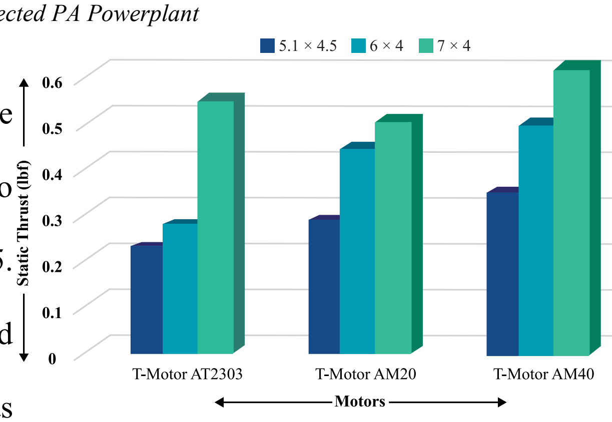

Figure 7.2 PADA TMD Results

A comparable approach was employed in selecting the motor and propeller for the PADA. The objective was to achieve a thrust-to-weight ratio within 0.55-0.65. Following physical testing, the T-MOTOR AM40 paired with an APC 7x4SF propeller was chosen. Power was provided by a 300mAh 2S 45C Li-Po battery. Toroidal propellers were also considered for the PADA, however, physical testing on a 5.1x4.5-inch propeller revealed that a traditional propeller of the same specifications provided 56.25% higher thrust. This showed that the advantages of toroidal propellers were not universal. It was found that they performed better in dense fluids and at specific speeds. Hence after careful consideration, traditional propellers were used.

Motor Selected	Kv	Static Thrust (lbf)	RPM	Propeller
T-Motor AM40	1500	0.6	8870	APC 7 × 4SF

Table 7.2 Characteristics of Selected PADA Powerplant

8. Manufacturing

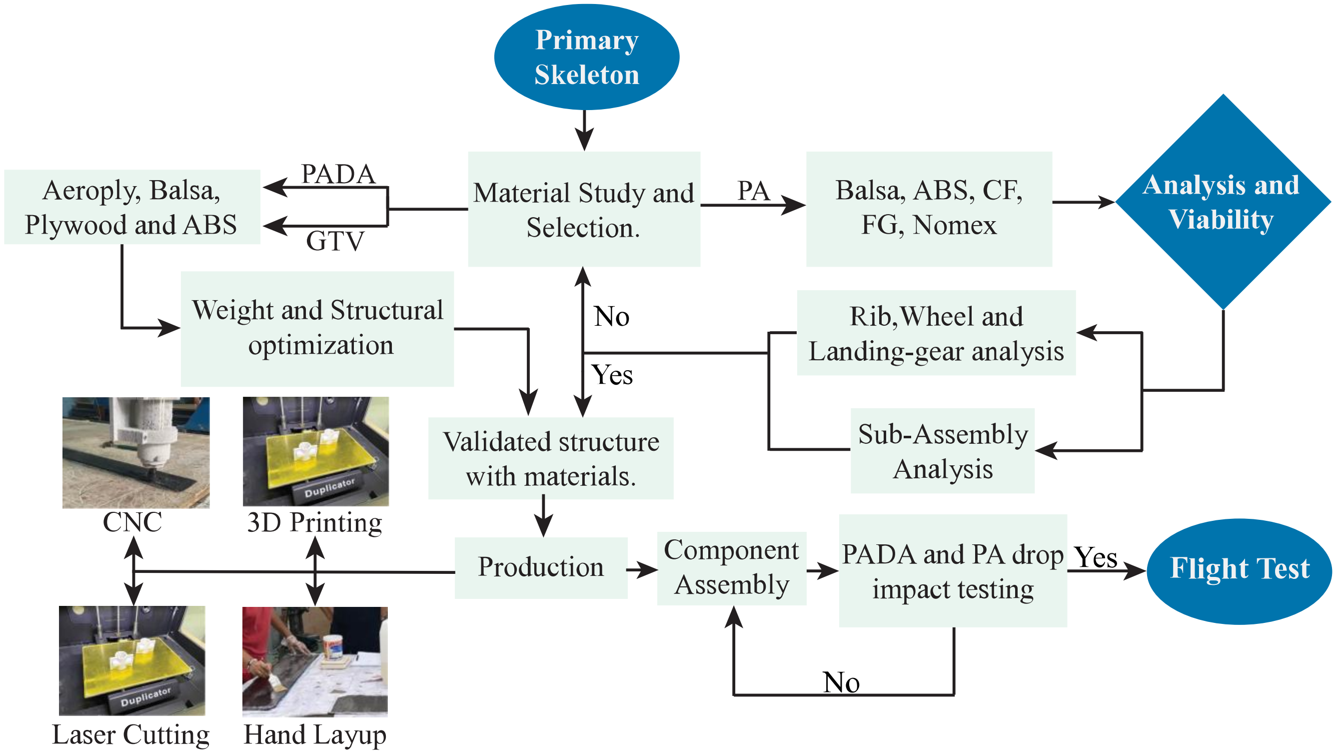

Figure 8.1 Manufacturing Plan

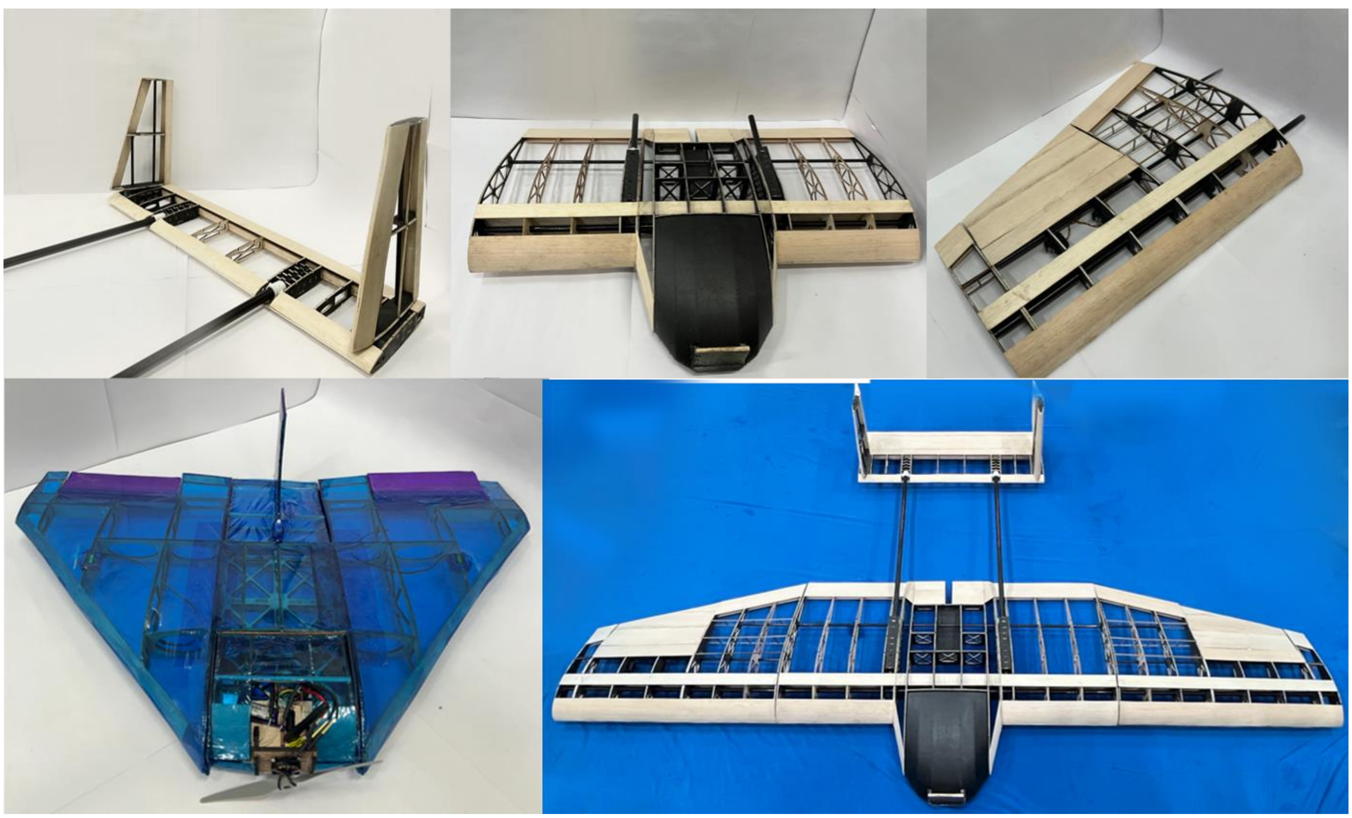

Figure 8.2 Manufacturing Images

9. Conclusion

Marut used a systems engineering approach in its design, manufacturing, and testing stages, which ensured the team's set objectives were successfully met for SAE Aero Design East 2024. Adhering to the scoring analysis, the team successfully developed an optimal design that was subject to meticulous examination. The utilization of fiber-reinforced composites and weight-minimizing methods contributed to achieving an equilibrium between strength, weight, and cost. The optimization of the thrust-to-weight ratio was achieved through appropriate selection of the powerplant. Test flights affirmed the efficiency of the autonomous system and verified minimal deviations in the PADA landings. As an autonomous system, the GTV carried water efficiently while keeping weight to a minimum.

Figure 9.1 Marut

10. References

[1] Mulh, J. 2022. Low-Speed Aerodynamic Characteristics of a Delta Wing with Articulated Wingtips, Elevons, and Leading-Edge Vortex Flaps: Doctoral dissertation, The Ohio State University.

[2] Nicolosi, F., Ciliberti, D., Della Vecchia, P., Corcione, S., & Cusati, V. 2017. A Comprehensive Review of Vertical Tail Design: Aircraft Engineering and Aerospace Technology

[3] Anderson, J.D. 1978. Introduction To Flight.

[4] Sadraey, M. H. 2012. Aircraft design: A systems engineering approach. John Wiley & Sons.

[5] Nelson, R.C. 1989. Flight Stability And Automatic Control. Iowa State University.

[6] Moorhouse, D. J., & Woodcock, R. J. (1982). Background Information and User Guide for MIL-F-8785C, Military Specification: Flying Qualities of Piloted Airplanes.

[7] Nicolosi, F., Della Vecchia, P., Ciliberti, D., & Cusati, V. (2016). Fuselage aerodynamic prediction methods. Aerospace science and technology, 55, 332-343.

[8] Zyskowski, M. (1995). Incorporating biplane wing theory into a large, subsonic, all-cargo transport. In Aircraft Engineering, Technology, and Operations Congress (p. 3918).

TEAM ASSAILING FALCONS
TEAM NUMBER 216
VELLORE INSTITUTE OF TECHNOLOGY
SCALE - 1:17 ALL DIMENSIONS ARE IN INCHES

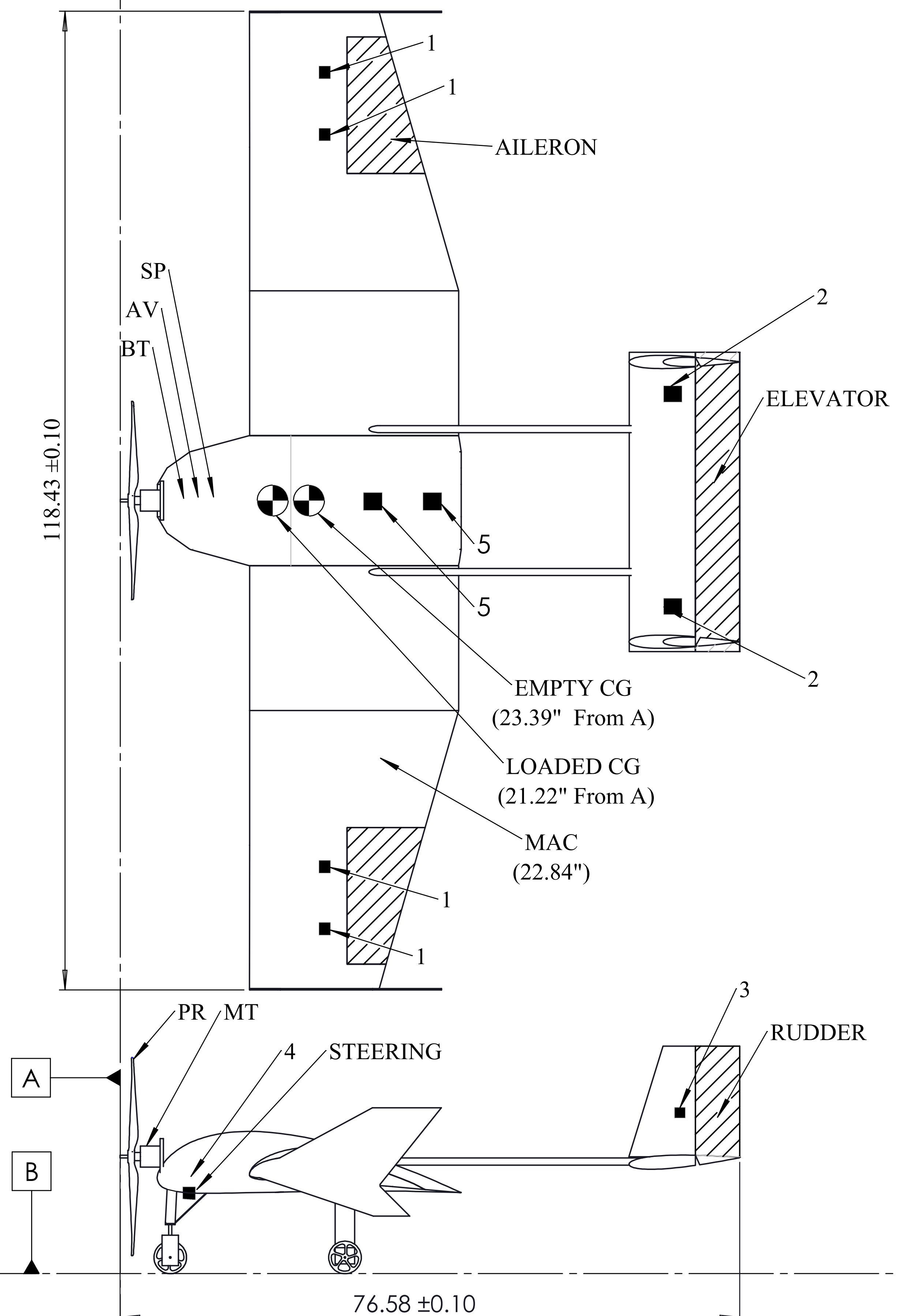

SUMMARY DATA

WINGSPAN	118.43 in
WING AREA	2278.51 in^2
ASPECT RATIO	4.61
EMPTY WEIGHT	20.06 lbs
BATTERY CAPACITY	5000mAh*1 1000mAh*1
MOTOR (MT)	SCORPION A-5524
MOTOR KV	205KV
PROPELLER(PR)	APC 24*12E
SERVO	1) HITEC HS-5645MG (168 oz-in) 2) HITEC D-625MW (122 oz-in) 3) HITEC HS-5496MH (89 oz-in) 4) HITEC D-951TW (403 oz-in) 5) HITEC D-145SW (68 oz-in)
MAC	22.83 in
EMPTY STABILITY MARGIN	4.69%
LOADED STABILITY MARGIN	14.17%
EMPTY CG	23.39 in
LOADED CG	21.22 in

DIMENSIONS

LENGTH	76.58 ± 0.10 in
WIDTH	118.43 ± 0.10 in
HEIGHT	24.48 ± 0.10 in

WEIGHT AND BALANCE INFORMATION

COMPONENT	ABBREVIATION	FORCE (lbf)	DISTANCE FROM DATUM A (in)	MOMENT (lbf-in)
MOTOR	MT	1.59	3.64	5.79
BATTERY	BT	1.91	9.24	17.65
STATIC PAYLOAD	SP	13.23	14.64	193.69
AVIONICS	AV	5.48	7.34	40.22
PADA	PD	1.00	32.43	32.43

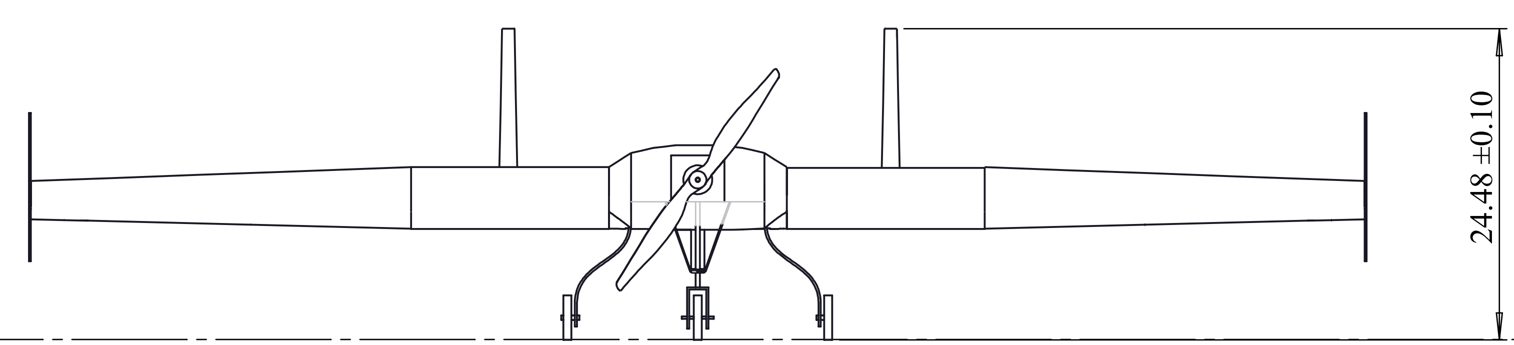

TEAM ASSAILING FALCONS

TEAM NUMBER 216

VELLORE INSTITUTE OF TECHNOLOGY

SCALE - 1:5 ALL DIMENSIONS ARE IN INCHES

VERTICAL DATUM LINE = A
HORIZONTAL DATUM LINE = B

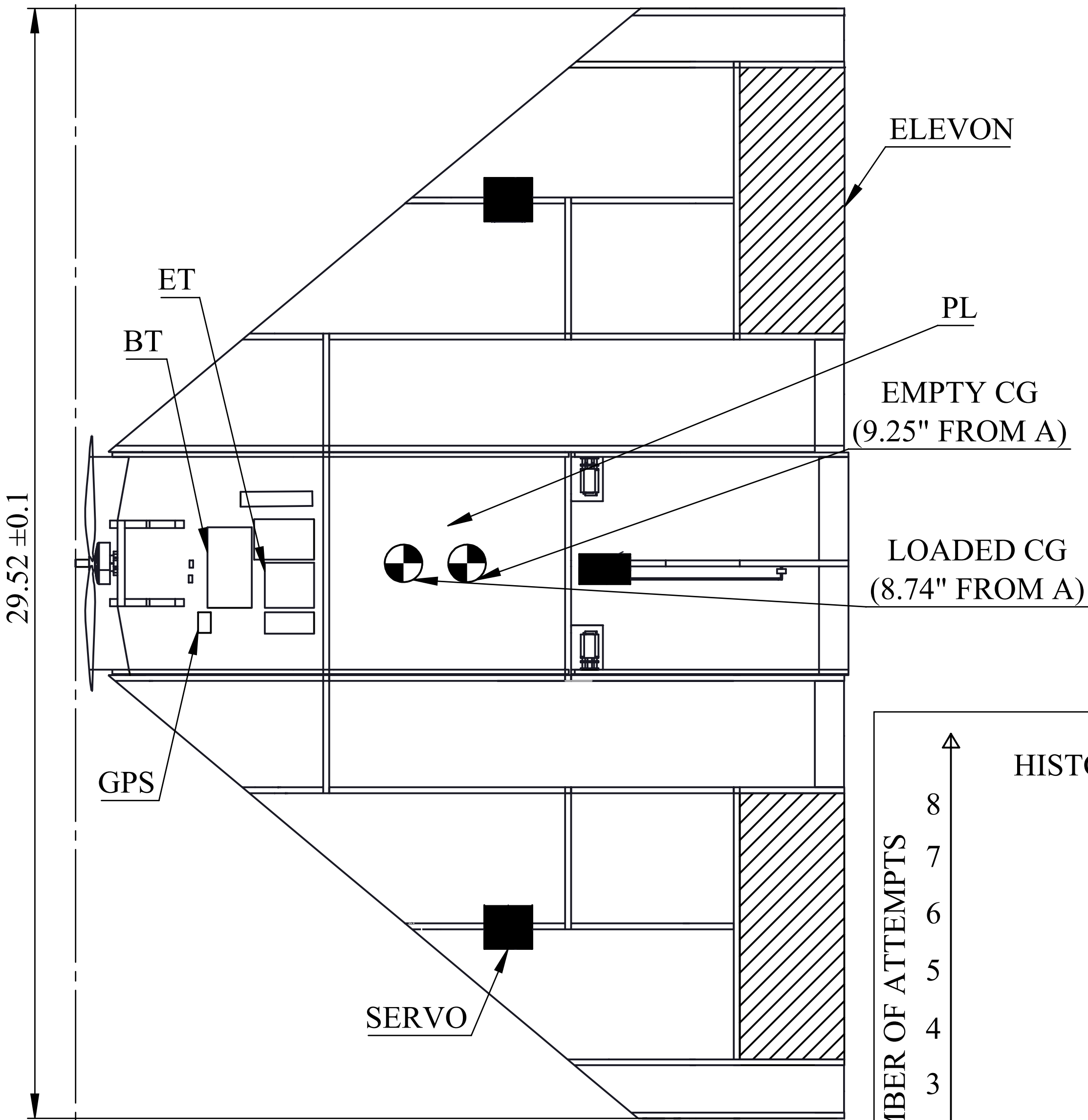

DIMENSIONS

LENGTH	29.52±0.1 in
WIDTH	19.69±0.1 in
HEIGHT	7.67±0.1 in

LIST OF AVIONICS AND EQUIPMENT

COMPONENTS	QUANTITY
GPS: NANO UBLOX M8 5883	1
FLIGHT CONTROLLER: KAKUTE F4 V2 Mini	1
MOTOR	1
ESC: BL Heli GS 30A 2-4S	1
LiPo BATTERY: 300mAh 45C 2S	1
RECEIVER	1
SERVOS	3

WEIGHT AND BALANCE INFORMATION

COMPONENTS	ABBREVIATION	FORCE (lbf)	DISTANCE FROM DATUM A (in)	MOMENT (lbf-in)
MOTOR	MT	0.04	0.92	0.03
BATTERY	BT	0.05	4.11	0.20
PAYLOAD	PL	0.12	9.90	1.18
ELECTRONICS	ET	0.28	3.52	0.98

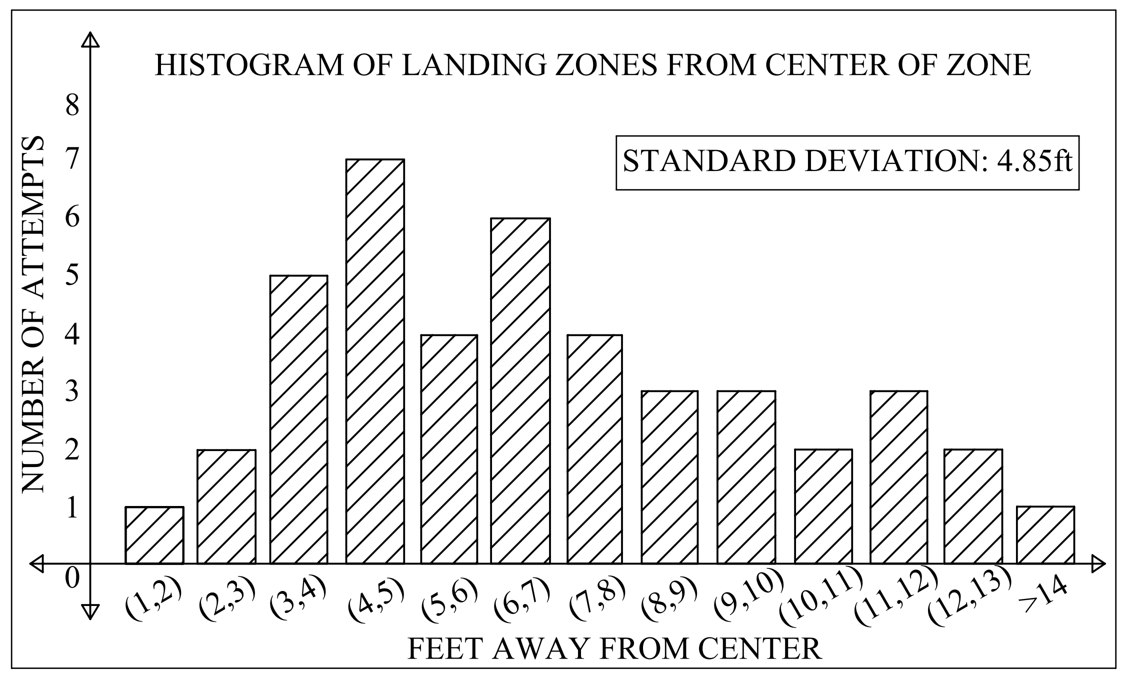

SUMMARY DATA

EMPTY WEIGHT	0.50 lbs
BATTERY CAPACITY	300mAh
MOTOR MAKE, MODEL AND KV	T-MOTOR, AM40, 1500KV
PROPELLER (PR) MANUFACTURER	APC
PROPELLER DIAMETER AND PITCH	7X4SF
SERVO MANUFACTURER	TECHTONICS
SERVO MODEL NUMBER	GH-S37D
SERVO TORQUE AT 4.8V	9.72 oz-in
MAC	15.35 in
EMPTY STABILITY MARGIN	16.8%
LOADED STABILITY MARGIN	17.1%
EMPTY CG	9.25 in
LOADED CG	8.74 in